# Efficient Removal of Per- and Polyfluoroalkyl Substances from Water with Zirconium-based Metal-Organic Frameworks

Rui Li<sup>1</sup>, Shefa Alomari<sup>2</sup>, Robert Stanton<sup>3</sup>, Megan C. Wasson<sup>4</sup>, Timur Islamoglu<sup>4</sup>, Omar K. Farha<sup>4,6</sup>, Thomas M. Holsen<sup>5</sup>, Selma Mededovic Thagard<sup>1</sup>, Dhara J. Trivedi<sup>3\*</sup>, and Mario Wriedt<sup>2\*</sup>

<sup>1</sup>Department of Chemical and Biomolecular Engineering, Clarkson University, Potsdam, New York 13699, United States

<sup>2</sup>Department of Chemistry & Biomolecular Science, Clarkson University, Potsdam, New York 13699, United States

<sup>3</sup>Department of Physics, Clarkson University, Potsdam, New York 13699, United States

<sup>4</sup>International Institute of Nanotechnology, Department of Chemistry, Northwestern University, Evanston, Illinois 60208-3113, United States

<sup>5</sup>Department of Civil and Environmental Engineering, Clarkson University, Potsdam, New York 13699, United States

<sup>6</sup>Department of Chemical and Biological Engineering, Northwestern University, Evanston, Illinois 60208-3113, United States

# Corresponding author contacts:

MW, email: <a href="mwriedt@clarkson.edu">mwriedt@clarkson.edu</a>; phone: 315-268-2355

DJT, email: dtrivedi@clarkson.edu; phone: 315-268-2398

#### **ABSTRACT**

Per- and polyfluoroalkyl substances (PFAS) are an emerging class of contaminants raising increased levels of concern due to their toxic, bioaccumulative, and persistent nature. Current solutions for removing PFAS from contaminated water rely on adsorption-based methods where commonly used sorbents, e.g. activated carbons and ion-exchange resins, exhibit low adsorption capacity and long equilibration time. Motivated by the generally deficient performance of these current materials, this work addresses the need for the discovery of advanced sorbents for high capacity and efficient PFAS removal. The zirconium-based metalorganic framework (MOF) NU-1000 was characterized for the adsorption of three perfluorosulfonic acids (PFSAs, C4-C8) and six perfluorinated carboxylic acids (PFCAs, C1-C9) from aqueous solution. Results indicate that NU-1000 exhibits outstanding adsorption capacities of 400-620 mg/g for PFSAs and 201-604 mg/g for PFCAs coupled with ultrafast adsorption kinetics featuring equilibrium times of <1 min. Complementary density functional theory calculations reveal that the PFAS@MOF adsorption mechanism is dominated by a combination of hydrogen bonding, electrostatic, and hydrophobic non-covalent PFAS— MOF interactions. Excellent regeneration and reusability characteristics were found, particularly nearly quantitative removal and recovery rates of NU-1000 after five consecutive ad- and desorption cycles of PFAS. Additional adsorption testing using PFAS-contaminated groundwater samples obtained from U.S. Air Force bases revealed impressive PFAS removal rates of 75-98% within 10 min regardless of the presence of co-contaminants. To the best of our knowledge, the suite of herein presented PFAS sorption characteristics—capacity, kinetics, regeneration and reusability—significantly outperforms other current sorbents; rendering NU-1000 as a promising platform for the rapid and effective removal of PFAS from aqueous media.

#### INTRODUCTION

Per- and polyfluoroalkyl substances (PFAS) are emerging contaminants composed of fluoroalkyated chains and hydrophilic functional groups.<sup>1</sup> Due to their excellent tensioactive properties and thermal and chemical stabilities, PFAS have a wide array of industrial and commercial applications<sup>2</sup> while the disposal of PFAS-containing products leads to the ubiquitous detection of PFAS compounds in drinking water, groundwater and surface water.<sup>3</sup> For example, the receiving rivers of the semiconductor industry wastewater<sup>4</sup> and groundwater near U.S. Air Force training facilities<sup>5</sup> may contain μg/L and mg/L contamination levels of PFAS, respectively. Considering the environmentally persistence, toxic and bioaccumulative nature of PFAS, numerous efforts have been devoted to the removal of PFAS from waterbodies including adsorption, filtration, reverse osmosis, enhanced photolysis, electrochemical oxidation, sonochemical destruction, etc.<sup>6</sup> However, many of these methods are expensive due to high energy requirements or exhibit low removal efficiency.

Adsorption-based technology using activated carbons and ion-exchange resins is the most commonly employed solution to treat PFAS contaminated waters to date, but these sorbents generally feature low PFAS adsorption capacities coupled with slow kinetics and/or low regeneration performance. In addition, the application of these media can be challenging due to the presence of organic matter (concentrations vary widely depending on water sources), and difficulties related to the treatment of shortchain (e.g., C4-C7) PFAS compounds.<sup>7</sup> Short-chain compounds are of particular interest because there is great concern regarding their mobility and potential health effects.<sup>8-10</sup> Treatment options have been investigated but standard processes are still ineffective to date.<sup>3,11</sup> PFAS adsorption of most media is chainlength dependent with adsorption capacities significantly lower for shorter-chain compounds and complicated by long equilibrium times for the adsorption process.<sup>12-13</sup> Therefore, more efficient solutions (i.e., regenerable sorbents with high adsorption capacities and fast uptake kinetics) for remediating a wide range of PFAS under various contaminated water quality conditions, with particular focus on short-chain compounds, are urgently needed.

Metal-organic frameworks (MOFs) are a new class of hybrid crystalline nanoporous materials, which are composed of inorganic and organic building blocks to form multidimensional frameworks. Their key features of ultra-large BET surface areas (up to ~7,310 m²/g)¹⁴ and pore volumes (up to ~3.9 cm³/g)¹⁵, combined with their tunable pore dimensions (pore sizes up to 10 nm)¹⁶ and functionalities, render MOFs as ideal candidates for adsorption-based applications with fast diffusion and kinetics. For example, MOFs have been proposed as sorbents for air purification¹७ and water purification,¹¹⁵ metal ion decontamination and the removal of chemical warfare agents.²⁰ However, to date, only very few studies have probed their

ability to sorb PFAS, 4, 21-23 e.g., a series of microporous Zn-based zeolitic imidazolate-based MOFs for the removal of perfluorooctanoic acid (PFOA),<sup>24</sup> Cr-based mesoporous MIL-101 derivatives for the removal of PFOA,<sup>21</sup> and the Th-based mesoporous framework SCU-8 for the removal of perfluorooctane sulfonate (PFOS).<sup>25</sup> Table S1 summarizes the PFAS adsorption performance of all MOF materials tested to date. These materials generally exhibited limited hydrolytic stability<sup>24</sup> with only partial regeneration of the material in successive cycles. In addition, their performance on short-chain PFAS is unknown.<sup>21, 25</sup> Motivated from these previous studies we considered zirconium-based MOFs as a potentially better choice for PFAS removal due to their generally remarkable hydrolytic, thermal and mechanical stabilities. 19, 26-28 In particular, we focused our work on MOF  $[Zr_6(\mu_3-O)_4(\mu_3-OH)_4(H_2O)_4(OH)_4(tbapy)_2]_n$  (tbapy = 1,3,6,8-(p-benzoate)pyrene), also known as NU-1000.<sup>29-30</sup> This MOF presents as a good candidate because of its heteroporous nature featuring one-dimensional hexagonal mesopore channels (~33 Å ø) and onedimensional triangular micropore channels (~13 Å ø). Both pores are connected by 8 × 10 Å windows which extend throughout the structure to facilitate rapid flow of substrates throughout the entire heterogeneous framework. In addition to the NU-1000's outstanding thermal and chemical stability, it is envisioned that the four terminally bonded anionic hydroxo ligands of the eight connected Zr<sub>6</sub>(µ<sub>3</sub>-O)<sub>4</sub>(µ<sub>3</sub>-OH)<sub>4</sub>(H<sub>2</sub>O)<sub>4</sub>(OH)<sub>4</sub> node would facilitate ion exchange reactions with anionic PFAS compounds. These characteristics motivated our interest in investigating NU-1000 for its PFAS removal capacities which we report herein.

#### RESULTS AND DISCUSSION

PFAS adsorption capacity, kinetics, and isotherms. Adsorption of nine PFAS compounds by NU-1000 were evaluated individually including three perfluorosulfonic acids (PFSAs) with carbon chain length of 4, 6, and 8; and six perfluorinated carboxylic acids (PFCAs) with carbon chain length of 1, 3, 4, 6, 7, and 9. The structures and compositions of respective perfluoroalkyl acids (PFAAs) are listed in **Table S2**. The results demonstrate that NU-1000 exhibits a large capacity for the adsorption of PFAA with ultra-short equilibrium times. **Table 1** provides a comprehensive overview of these adsorption characteristics showing that the adsorption capacity of C1-C8 PFAAs is in the range of 201-622 mg/g (1.2-1.8 mmol/g, 2.4-3.6 molecules/Zr<sub>6</sub> node of NU-1000). A comparison of these data with commonly used adsorbents listed in **Table S3** (e.g., adsorption capacities range 40-170 mg/g for commercial activated carbons and resins) reveals that NU-1000 is one of the highest-capacity PFAS adsorption material, making it a superior adsorbent for short- and long-chain PFAAs. Additional comparative adsorption testing was performed using perfluorobutanesulfonic acid (PFBS) with commercial granular and powdered activated carbons under the same experimental conditions. PFBS is selected as representative model compound for this testing (and others as described below) due to its significant

environmental relevance since short-chain PFAS are widely used as alternatives to long-chain PFAS. The results are listed in **Table S4** and reveal an adsorption capacity of 404 mg/g for NU-1000, which is two orders of magnitude higher than the commercial adsorbents. The adsorption performance of NU-1000 was further probed using a complex PFAS mixture at environmentally relevant concentrations (i.e., PFAS concentrations typically found in contaminated groundwater). Per **Table S5**, the lab-prepared mixture was composed of eight different PFAAs with individual concentrations ranging between 90 and 423  $\mu$ g/L. The adsorption testing results displayed in **Figure 1** reveal individual removal efficiencies in the 90-100% range.

Adsorption kinetics is commonly described using a pseudo-second order model. However, the PFAS adsorption kinetics by NU-1000 cannot be determined due to the ultrafast equilibrium time of <1 min for most analyzed PFAS, as evident from the time-dependent concentration profiles shown in **Figures S1-S3**. NU-1000 significantly outperformed conventional and emerging PFAS adsorbing materials, which usually require >2 h to reach respective adsorption capacities.<sup>1, 7, 31-32</sup>

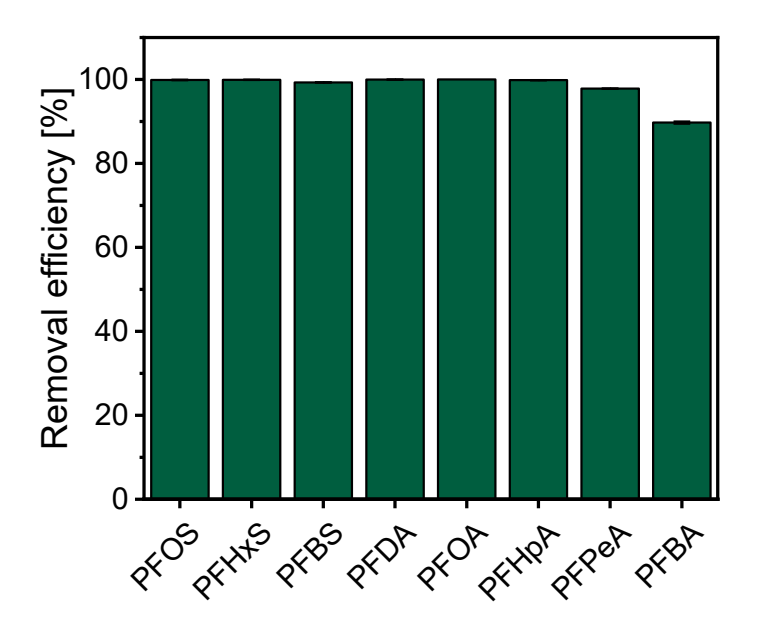
Adsorption isotherm studies were performed using PFBS as a representative model compound. **Figure S4** displays the adsorption capacities of NU-1000 at different PFBS concentrations with respective Langmuir and Freundlich fits. The high R<sup>2</sup> values of the fits reveal classical Langmuir and Freundlich adsorption behavior. Employing the Langmuir equation suggests that PFBS is adsorbing on NU-1000 in a monolayer fashion at a single adsorption site, while the goodness of the Freundlich equation fit suggests that the surface is heterogenous with PFBS adsorbing with different adsorption energies at multiple adsorption sites. The high adsorption capacity with fast kinetics is attributed to the MOFs' high surface area, favorable electrostatic and hydrophobic interactions between the MOF and PFAS, which will be discussed in detail in the following section.

Table 1. Adsorption capacities and equilibrium times of different PFCAs and PFSAs by NU-1000.

PFAS C-F chain length			Ad	Equilibrium time		
			[mg/g]	[mmol/g]	[molecules/ Zr <sub>6</sub> node] <sup>b</sup>	[min]
PFSA	PFOS	8	$622 \pm 10$	$1.24 \pm 0.02$	2.5	1
	<b>PFHxS</b>	6	$547\pm28$	$1.37\pm0.07$	2.8	1
	PFBS	4	$404\pm33$	$1.35\pm0.11$	2.8	1
PFCA	PFDA	9	$604 \pm 15$	$1.17\pm0.03$	2.4	1
	PFOA	7	$507\pm33$	$1.22\pm0.08$	2.5	1
	PFHpA	6	$421\pm17$	$1.16 \pm 0.05$	2.5	1
	PFPeA	4	$344\pm12$	$1.30 \pm 0.05$	2.7	5
	PFBA	3	$274\pm25$	$1.28 \pm 0.12$	2.6	10
	TFA	1	$201\pm17$	$1.76 \pm 0.15$	3.6	1

<sup>a</sup>Experimental conditions: 10 mg of NU-1000 was exposed to 50 mL of 100 mg/L individual PFAS solutions. Equilibrium times were experimentally observed based on sampling time which, noteworthy, cannot be measured <1 min due to restrictions of experimental set-up. All standard deviations of the adsorption capacity are within 10% for all PFAS.

<sup>b</sup>Details on unit calculations are provided in SI.



**Figure 1.** Removal efficiencies of individual PFAS compounds from a lab-prepared mixture solution. Error bars are not visible due to their small values. Experimental conditions: 10 mg of NU-1000 was exposed to 50 mL of PFAS mixture with individual PFAS concentration of ~0.1 mg/L. See Table S5 for detailed mixture composition.

**Mechanism of the PFAS@NU-1000 adsorption process.** Multiple mechanisms can be responsible for the PFAS adsorption onto NU-1000. Per **Table 1**, the maximum adsorption capacity of PFAS follows the order PFOS>PFHxS>PFBS for PFSAs and PFDA>PFOA>PFHpA>PFPeA>PFBA>TFA for PFCAs, indicating the higher affinity of NU-1000 for longer chain PFAS due to increasing hydrophobic PFAS@NU-1000 interactions with increasing C-F chain length. With the same C-F chain length, the adsorption capacity of sulfonic acids exceeds that of carboxylic acids due to significant differences in their pK<sub>a</sub> values (e.g., -3.3 for PFBS and -2.3 for PFPeA). Accordingly, at a given pH, the concentration of ionized PFSAs is higher than that of PFCAs which facilitates electrostatic PFAS@NU-1000 interactions of PFSA over PFCA. This

observed chain length and functional group dependences for PFAS adsorption on NU-1000 is in accordance with the mechanisms established for activated carbons and ion exchange resins.<sup>12</sup>

Subsequent characterization including scanning electron microscopy (SEM), powder X-ray diffraction (PXRD), physisorption analysis (BET surface area and DFT pore size distribution), Fourier-transform infrared spectroscopy (FTIR), diffuse reflectance infrared Fourier-transform spectroscopy (DRIFTS), and X-ray photoelectron spectroscopy (XPS) provided fundamental insights into the PFAS@NU-1000 adsorption process. The short-chain PFBS was selected as a representative model compound for this mechanistic study. The crystal structure of PFBS is shown for reference in **Figure 2A** and respective characterization data before and after PFBS adsorption into NU-1000 are displayed in **Figures 2B-2F**, **S5** and **3**. The morphology of NU-1000 crystallites after PFBS adsorption remains unchanged as evident from respective SEM images shown in **Figure S5** while the structural integrity of NU-1000 after PFBS adsorption is evident from the absence of any additional Bragg reflections comparing the PXRD pattern of PFPBS@NU-1000 vs. the calculated pattern of NU-1000 as shown in **Figure 2B**. In addition, the peak intensity of the (100) reflection significantly decreased compared to NU-1000, which is attributed to a progressive phase cancellation phenomenon associated with the introduction of scattering material into the pore system.<sup>33-35</sup>

Similar characteristics are evident from changes in the Brunauer-Emmett-Teller (BET) specific surface areas and density-functional theory (DFT) pore-size distributions; both derived from  $N_2$  adsorption isotherms at 77 K of NU-1000 before and after PFBS adsorption. **Figure 2C** shows that the  $N_2$  adsorption capacity of pristine NU-1000 (1017 cm<sup>3</sup>/g) is almost double the value as compared to PFBS@NU-1000 (635 cm<sup>3</sup>/g) at  $p/p_0$  of ~1 with the respective calculated BET surface area decreasing from 2255 to 1608 m<sup>2</sup>/g. The change in the pore volume from 1.56 to 0.98 cm<sup>3</sup>/g follows a similar trend, as revealed by the DFT pore-size distribution plots shown in **Figure 2D**. These findings are consistent with PFBS molecules occupying the pore space of NU-1000. The mor

FTIR and DRIFTS were employed to obtain insights into the PFBS adsorption mechanism. The FTIR spectra of NU-1000 before and after PFBS adsorption are plotted in **Figure 2E**. The spectrum for pristine NU-1000 features a broad and sharp band at 3350 and 1410 cm<sup>-1</sup> respectively, representing O—H stretching and bending modes respectively, which are characteristic for the terminally bonded anionic hydroxo ligands of the Zr<sub>6</sub>(μ<sub>3</sub>-O)<sub>4</sub>(μ<sub>3</sub>-OH)<sub>4</sub>(H<sub>2</sub>O)<sub>4</sub>(OH)<sub>4</sub> node. After PFBS adsorption, these bands vanished, and a group of sharp bands between 1400-1000 cm<sup>-1</sup> and a sharp band at 1360 cm<sup>-1</sup> appeared, which respectively correspond to C—F and S=O stretching modes. The FTIR spectrum is consistent with the spectral characteristics of PFBS, and in particular, it demonstrates that the sulfonyl groups of the PFBS deprotonate during the adsorption process in aqueous media. The resulting sulfonate groups coordinate to

the Zr<sub>6</sub>-node by replacing the original terminally coordinated hydroxo ligands. Thus, indicating that SO<sub>3</sub>— Zr coordinative bonding is the key feature of the PFBS@NU1000 adsorption mechanism. This conclusion is further corroborated by the DRIFTS spectra displayed in **Figure 2F** showing a high-intensity sharp band at 3672 cm<sup>-1</sup> for pristine NU-1000, indicative of the O—H stretching mode of the Zr<sub>6</sub>-node's hydroxo ligands.<sup>36</sup> For PFBS@NU-1000, this band is broadened and reduced in intensity upon red shifting to 3653 cm<sup>-1</sup>. This observation suggests changes in the electronic structure of the Zr<sub>6</sub>-node which originate from the PFBS@NU-1000 adsorption process (*i.e.*, hydroxo *vs.* sulfonate ion exchange reaction).<sup>36</sup>

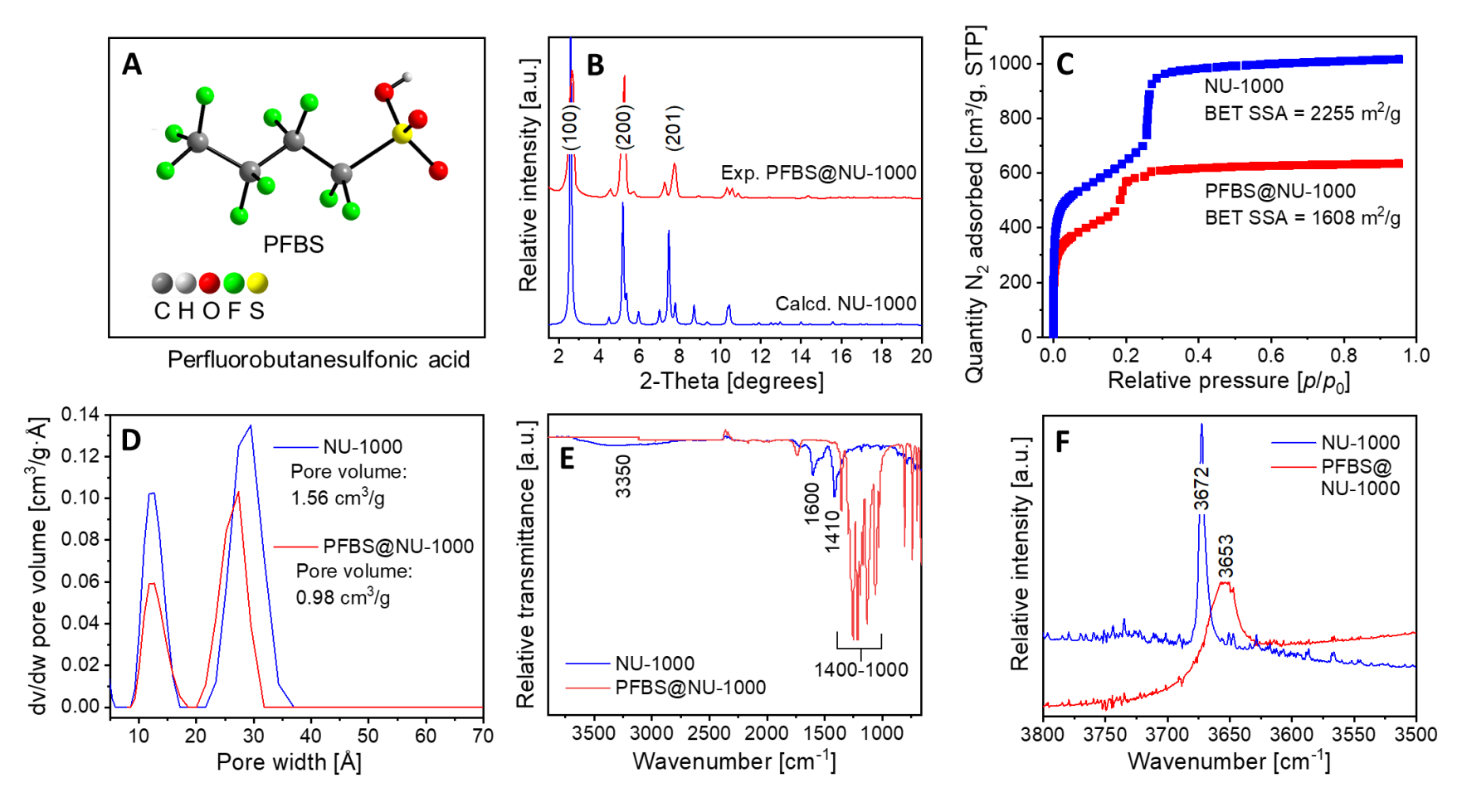
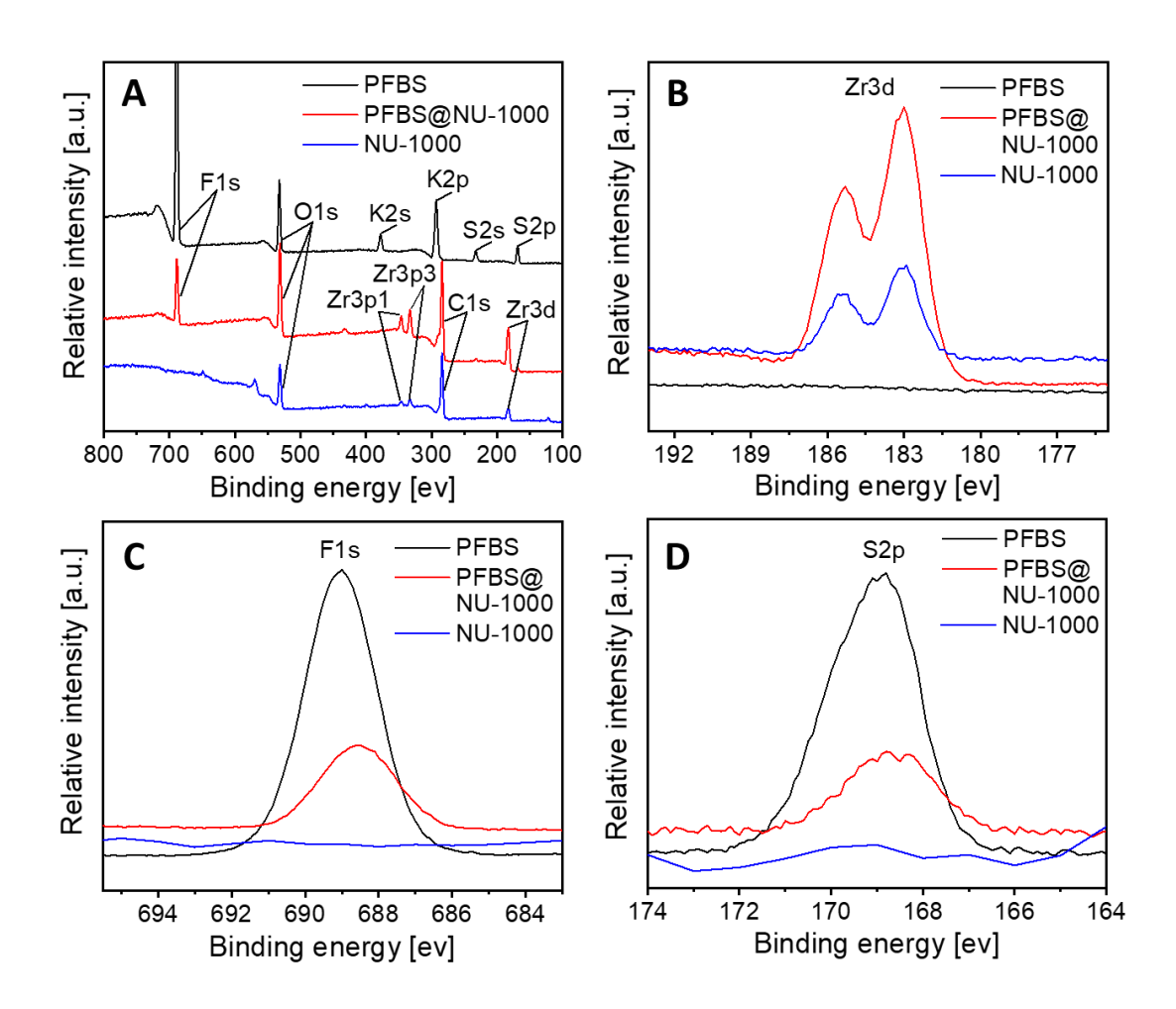


Figure 2. Structural characterization of NU-1000 before (blue) and after (red) saturation with PFBS: (A) crystal structure of PFBS for reference; (B) PXRD patterns; (C) N<sub>2</sub> adsorption isotherms at 77 K with respective BET surface areas, desorption points omitted for the sake of clarity; (D) DFT pore size distribution plots with respective pore volumes; (E) FTIR spectra. For reference, the band at 1600 cm<sup>-1</sup> represents C=O from residual DMF molecules of as-synthesized NU-1000, DMF is washed off after PFBS adsorption in water; and (F) DRIFTS spectra. All MOF samples were thoroughly dried before spectra collection to avoid any interference with residual water molecules.

XPS was employed to analyze the surface changes of NU-1000 upon PFBS adsorption. The XPS survey scans of NU-1000, PFBS and PFBS@NU-1000 are presented in **Figure 3A** and summarized in **Table S6. Figures 3B-D** show high-resolution scans of Zr 3d, F 1s, and S 2p binding energies, respectively. NU-1000 exhibits characteristic Zr 3d peaks located at 185.3 and 183.0 eV which indicate the existence of Zr<sup>4+</sup>. For PFBS, the peaks at 689.0 and 269.0 eV match the F 1s and S 2p binding energies, respectively, which are consistent with oxidation states of -1 for fluorine and +4 for sulfur. Upon PFBS@NU-1000 formation, F 1s and S 2p binding energies for PFBS are found at 688.5 and 268.5 eV, respectively, while NU-1000 shows its characteristic Zr 3d binding energies at 185.3 and 183.0 eV. Notably, binding energies of PFBS are shifted to lower values by 0.5 eV, which agrees with the induced chemical changes of the trifluoromethyl and sulfonate groups due to adsorption on NU-1000. The Zr 3d peaks of NU-1000 remain unchanged during this process indicating no structural changes of the Zr<sub>6</sub> node. All these features confirm the successful PFBS adsorption into NU-1000.



**Figure 3.** XPS analysis for PFBS@NU-1000 (red) with pristine NU-1000 (blue) and PFBS (black) for reference: (A) survey, (B) Zr 3d, (C) F 1s, and (D) S 2p spectra. In the survey spectra of PFBS, the K 2s and K 2p peaks originate from the potassium salt of PFBS.

Comparative adsorption testing using different MOFs. Spectral characterizations revealed strong evidence that the PFAS adsorption mechanism is driven by an anion exchange reaction at the Zr<sub>6</sub> node of NU-1000. This finding suggests that only MOFs with a combination of suitable (i) porosity and (ii) node composition (i.e., pore sizes exceeding the kinetic diameter of PFAS, and cationic metal nodes featuring terminally coordinating anionic ligands) have the potential to exhibit significant PFAS adsorption capacities. To support this conclusion, we selected MOF-74<sup>37</sup>, UiO-66<sup>38</sup> and ZIF-8<sup>39</sup> for further PFAS adsorption testing using PFBS as a representative probe. These MOFs fulfill the porosity criteria featuring pore sizes of 11, 9 and 12 Å, respectively, but lack the node composition criteria, e.g.,  $\{Mg_3(-O)_3(-CO_2)_3(H_2O)_3]\}_{\infty}$  for MOF-74,  $[Zr_6(\mu_3-O)_4(\mu_3-OH)_4(-CO_2)_{12}]$  for UiO-66 and  $[Zn(-N)_4]$  for ZIF-8. The respective adsorption testing results are displayed in **Figure S6**. As expected, none of these MOFs shows any measureable PFBS adsorption even after a prolonged adsorption time of 30 min. Since a size exclusion-based mechanism can be ruled out, this finding provides further evidence that the PFAS adsorption in NU-1000 is dominated by an anion exchange mechanism.

Computational modeling of PFAS—NU-1000 interactions. NU-1000 shows higher affinity for longer chain PFAAs, while the adsorption capacity of sulfonic acids exceeds that of carboxylic acids with the same C-F chain length. Density functional theory (DFT) calculations were employed to investigate the origin of these adsorption characteristics. PFSAs PFBS (short-chain) and PFOS (long-chain), and PFCA PFPeA (short-chain) were selected as representative PFAS model compounds. PFAS molecules were introduced at two different adsorption sites in a solvated model of NU-1000 which have been previously identified as potential binding sites for guest molecules. <sup>40</sup> For reference, the composition of this solvated model is Zr<sub>6</sub>(μ<sub>3</sub>-O)<sub>4</sub>(μ<sub>3</sub>-OH)<sub>4</sub>(OH)<sub>4</sub>(tbapy)<sub>2</sub> with the terminally coordinating OH groups being replaced by PFAS. Resulting optimized structures of PFBS@NU-1000 are displayed in Figure 4; structures of PFOS@NU-1000 and PFPeA@NU-1000 in Figures S7 and S8; and key adsorption energy and bonding parameters are summarized in Table 2. Per Figure 4A, adsorptions sites 1 and 2 are located in the hexagonal mesopore and triangular micropore, respectively. The Zr<sub>6</sub> node at both sites features Zr-coordinated aqua ligands that enable hydrogen bonding interactions with PFBS, while unsaturated Zr sites promote additional electrostatic interactions and/or coordinative bonding. Further characteristics of the adsorption sites are

evident from Figures 4B and 4C which show different orientations of the MOF linker's pyrene motifs. At site 1, the pyrene motifs are orthogonally aligned towards the center of the site, while at site 2, parallel orientated pyrenes form a hydrophobic pocket. These structural characteristics result in the preferred adsorption of PFBS at site 2 as evident from calculated adsorption energies of -233.3 kJ/mol for site 1 and -336.0 kJ/mol for site 2. Adsorption of PFBS at site 1 is visualized in Figure 4D showing PFBS—NU-1000 bonding stabilized by strong H bonding interactions (RSO<sub>3</sub>···H—O, 1.74 Å, ∠174.1°) while electrostatic interactions (RSO<sub>3</sub>—Zr, 4.09 Å) and hydrophobic interactions (C-F chain—pyrene motif, ~6 Å) are negligibly weak. Per Figure 4E, PFBS adsorption at site 2 is dominated by strong coordinative bonding (RSO<sub>3</sub>—Zr, 2.46 Å) which is in line with the proposed anion exchange mechanism as derived from spectral data. In addition, PFBS is spatially confined by the two pyrene ligands at the vertex of the triangular pore featuring significant hydrophobic interactions (C-F chain—pyrene motif, ~4 Å) and moderate H bonding (RSO<sub>3</sub>···H—O, 1.84 Å, ∠153.7°). A similar trend in adsorption preference for site 2 is found for all tested PFAS compounds as evidenced from the calculated adsorption energies listed in Table 2; and noteworthy, the experimentally observed preferred adsorption of PFSA over PFCA compounds of the same chain length is also confirmed from calculated adsorption energies (e.g., -336.0 kJ/mol for PFBS and -275.1 kJ/mol for PFPeA). This finding is corroborated by optimized structures showing that PFSA adsorption is dominated by strong coordinative bonding (RSO<sub>3</sub>—Zr, <2.5 Å) which is absent for PFCA (RCOO—Zr, >>4 Å). The experimentally observed dependency of the C-F chain length vs. PFAS adsorption capacity remains inconclusive based on calculated adsorption energies which is unsurprising given that this dependency is based on relatively weak and complex hydrophobic van der Waals-based C-F chain—pyrene interactions.

**Table 2.** Key energy and bonding parameters of the PFAS@NU-1000 adsorption process.

PFAS		Adsorption site #a	C-F chain length	H bonding characteristics <sup>b</sup> PFAS···H—O [Å, deg]	Bond length <sup>c</sup> PFAS—Zr [Å]	Adsorption energy [kJ/mol]
PFSA	PFBS	1	4	1.74, 174.1	4.09	-233.3
	PFBS	2	4	1.85, 153.7	2.46	-336.0
	PFOS	1	8	1.69, 171.1	4.01	-239.9
	PFOS	2	8	1.78, 150.5	2.39	-335.5
PFCA	PFPeA	1	4	1.59, 174.3	4.35	-246.3
	PFPeA	2	4	1.56, 166.9	4.54	-275.1

<sup>&</sup>lt;sup>a</sup>Corresponding adsorption sites are depicted in Figure 4.

<sup>&</sup>lt;sup>b</sup>Defined as O<sub>PFAS</sub>···H<sub>water</sub> distance and O<sub>PFAS</sub>···H—O<sub>water</sub> angle.

<sup>&</sup>lt;sup>c</sup>Shortest O<sub>PFAS</sub>—Zr distance with the Zr<sub>6</sub> node.

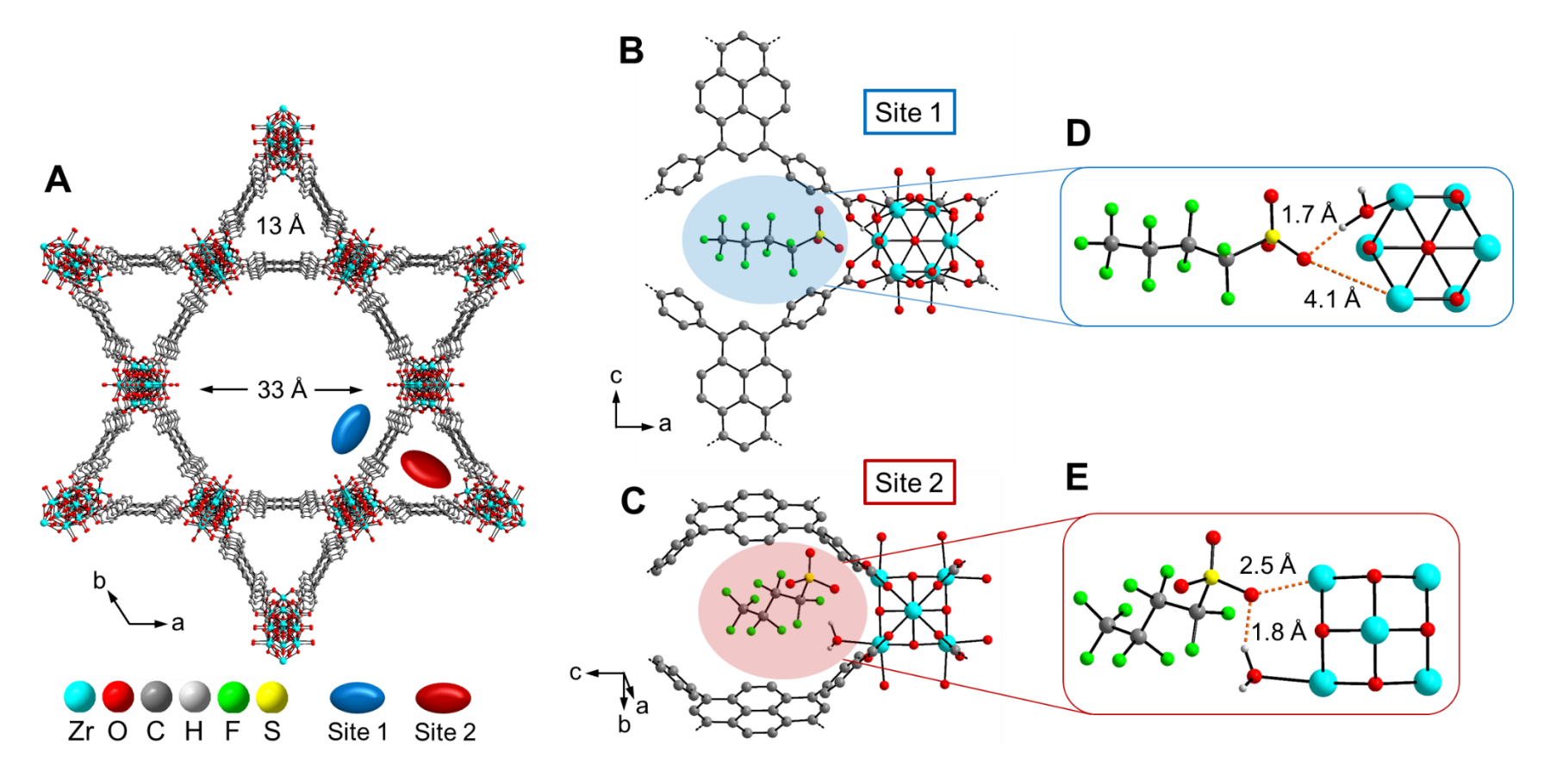


**Figure 4.** Structural characteristics of the PFBS@NU-1000 adsorption mechanism: (A) crystal structure of NU-1000 with view along the crystallographic *c*-axis showing the hexagonal meso- and triangular micropores with respective adsorption sites highlighted as colored ellipsoids; (B and C) DFT optimized geometries of PFBS—pyrene linker—Zr<sub>6</sub> node domains of PFBS@NU-1000 at adsorption sites 1 and 2, respectively; (D and E) zoomed-in view on respective adsorption sites with dashed lines representing hydrogen bonding and electrostatic interactions of the RSO<sub>3</sub>···H<sub>2</sub>O—Zr<sub>6</sub> and RSO<sub>3</sub>—Zr<sub>6</sub> motifs, respectively. All but water hydrogen atoms are omitted from structures for clarity.

**Regeneration of adsorbent.** Adsorbent regeneration is an important property required for sustainable and economical water treatment applications. Commonly used adsorbents for PFAS removal such as activated carbons show very limited regeneration capabilities, 12, 41 while MOF regeneration has been largely underexplored.<sup>21</sup> NU-1000 was screened for PFAS recovery using PFBS as the representative PFAS compound using a variety of different inorganic salt and solvent combinations (Figure S9). Pure methanol or 0.1 M HCl in water resulted in only limited recovery while a 30/70 (v/v) binary mixture of 0.1 M HCl in methanol was identified as the best performing desorption solution and selected for use in systematic regeneration studies. Figure 5 shows the removal and recovery rates of PFBS which were obtained from five successively performed adsorption and regeneration cycles using PFBS concentrations of 10 and 1000 mg/L, respectively. PFBS removal capacities ranging from 96 to 100% over five regeneration cycles were observed along with PFBS recovery rates ranging from 86 to 105% for samples of 10 mg/L PFBS concentration as displayed in Figures 5A and 5B. Similar trends are observed in Figures 5C and 5D for high concentration solutions containing 1000 mg/L PFBS. Adsorption capacities ranged from 355 to 419 mg/g over five cycles and were similar to NU-1000's PFBS maximum uptake capacity of  $404 \pm 33$  mg/g. PFBS recovery rates were between 98 and 117%. NU-1000 was characterized by PXRD and BET after successive regeneration cycling with respective data shown in Figures S10 and S11. The PXRD patterns show no loss of Bragg reflections after regeneration indicating the structural integrity of NU-1000 while a slight peak broadening of Bragg reflections might suggest some minor decrease in MOF crystallite sizes due to extensive tumbling in regeneration solvent. Respective BET surface areas show only minor decreases of ~4% (1 cycle) and ~6% (5 cycles) as compared to a control sample. In addition, the regeneration mechanism was probed by proton NMR spectroscopy using base-digested NU-1000 samples after (i) saturation with PFBS, (ii) regeneration with HCl/methanol mixture, and (iii) resaturation of a previously regenerated sample with PFBS. From NMR spectra displayed in Figure S12, it is evident that the regeneration process does not entail the coordination of methoxy groups after regeneration at the active sites of the Zr<sub>6</sub> node. This finding is different from a previous study by Grace et al.<sup>42</sup> which reported that the coordination of methoxy groups formed when NU-1000 is exposed to methanol. Consequently, the mechanism of PFBS@NU-1000 regeneration might proceed according to the HSAB theory involving chloride anions from the HCl/methanol mixture replacing coordinated PFBS at the Zr<sub>6</sub> node given the superior Cl—Zr coordination strength as compared to MeO—Zr and RSO<sub>3</sub>—Zr.

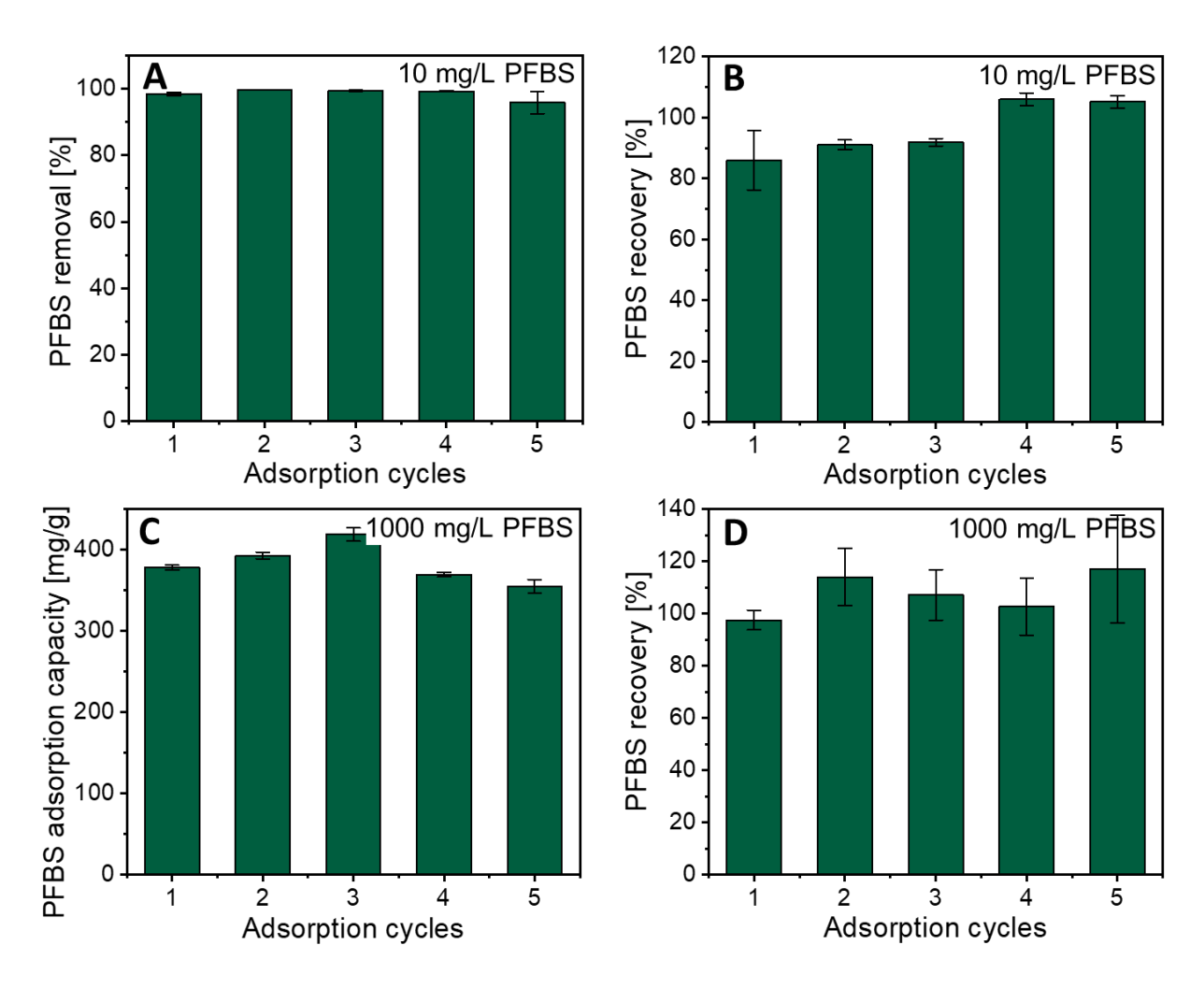


**Figure 5.** Regeneration characteristics of PFBS@NU-1000: (A and C) PFBS removal and (B and D) PFBS recovery rates of NU-1000 obtained from five successive adsorption and regeneration cycles using PFBS concentrations of (A and B) 10 mg/L and (C and D) 1000 mg/L, respectively. The recovery of PFBS is within the acceptance criteria of DoD (60-140%).

PFAS adsorption from contaminated groundwater samples. Contaminated groundwater samples obtained from four U.S. Air Force bases were used to investigate the impact of co-contaminants on PFAA sorption by NU-1000. These samples are denoted as liquid investigation-derived waste (IDW) and contained 11 PFAS compounds above detection limits (19-258 μg/L) with conductivities of 22-26,300 μS/cm. The detailed compositions of samples are listed in **Table S7** and individual PFAS removal capacities of NU-1000 are displayed in **Figure 6**. The total PFAS removal capacities range between 75 and 98% and that for individual PFAS mostly between 80 and 100% demonstrating high PFAS adsorption selectivity of NU-1000 in the presence of co-contaminants. Noteworthy, this trend deviates for short chain

PFAS compounds in samples IDW 1 and 2 due to their significantly higher conductivities as compared to samples IDW 3 and 4. This decreased removal is likely due to competitive coordinative binding of PFAS vs. highly concentrated inorganic salts (e.g., nitrates, sulfates and halides) with the Zr<sub>6</sub> node of NU-1000. This effect is less pronounced for longer chain PFAS in samples IDW 1 and 2 since hydrophobic interactions with NU-1000's pyrene motifs become more dominant. The kinetics of this competitive adsorption process are of fundamental interest but remain unclear due to experimental limitations to quantitatively assess the ultrafast second-scale equilibrium times of PFAS sorption. After exposure to the contaminated groundwater, all NU-1000 samples were characterized by PXRD, which revealed the unchanged structural integrity of the MOF as evident from **Figure S13**. Overall, the results demonstrate that NU-1000 shows outstanding performance for the treatment of PFAS contaminated groundwater.

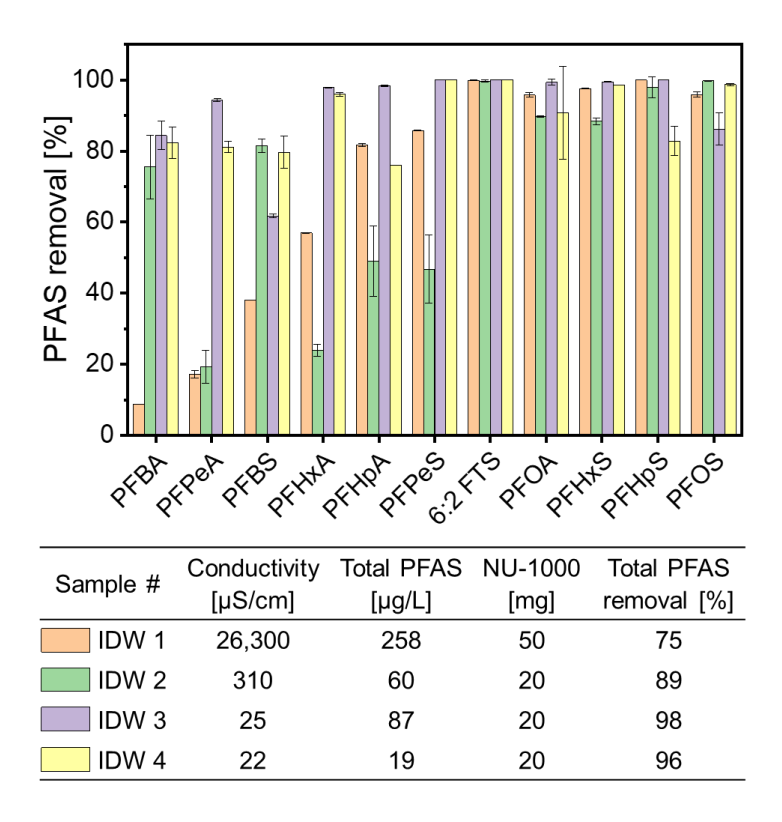


**Figure 6.** Removal capacities of PFAS from contaminated groundwater samples obtained from U.S. Air Force bases. The C-F chain length of PFAS compounds increases from left to right (e.g., 3 for PFBA and 8 for PFOS). The dosing of NU-1000 for sample IDW 1 is higher compared to samples IDW 2-4 due to its higher conductivity.

#### **CONCLUSIONS**

PFAS removal from contaminated water is a challenging process. State-of-the-art adsorbents lack reasonable PFAS removal capacities and/or show limited regeneration capabilities. In the present study, we demonstrate through systematic PFAA adsorption testing that NU-1000 is an effective sorbent for PFAS removal from aqueous media. NU-1000 has adsorption capacities of up to 620 mg/g for both long-chain and short-chain PFAAs with fast kinetics resulting in equilibrium times of <1 min. Preferred adsorption of PFSA over PFCA compounds and long- over short-chain PFAS compounds was observed. Adsorption testing was performed with nine different single PFAS compounds, laboratory-prepared complex mixtures, and for the first time in the field of MOFs, groundwater samples obtained from contaminated U.S. Air Force bases. The adsorption mechanism was probed by a suite of spectral methods revealing that PFAS adsorption is driven by strong ionic interactions with the eight-connected Zr<sub>6</sub> node of NU-1000. The fundamentals of these electrostatic interactions were further complemented DFT calculations, revealing that they are dominated by coordinative and hydrogen bonding as well as non-specific hydrophobic interactions. In addition, for the first time in the field of PFAS@MOFs, outstanding regeneration and reusability characteristics were demonstrated with near quantitative removal and recovery rates after five consecutive ad- and desorption cycles. All these performance characteristics render NU-1000 a promising hydrolytically stable adsorbent for water remediation featuring rapid and effective removal of PFAS and offer guidelines on next-generation sorbent design.

#### **EXPERIMENTAL SECTION**

Synthesis and general analytical techniques. All reagents and solvents were used without further purifications. Pristine samples of NU-1000 were synthesized as previously reported. PXRD patterns were recorded on a Bruker D2 Phaser diffractometer equipped with a Cu sealed tube ( $\lambda = 1.54178$  Å). Powder samples were dispersed on low-background discs for analyses. Gas adsorption isotherms for pressures ranging from  $1 \cdot 10^{-5}$  to 1 bar were collected volumetrically using a Micromeritics ASAP2020 surface area and pore analyzer. Warm and cold free-space correction measurements were performed for all isotherms using ultra-high-purity He gas (UHP grade 5.0, 99.999% purity). N<sub>2</sub> (99.999% purity) isotherms at 77 K were measured in liquid nitrogen. The samples were outgassed at 623 K for 12 hours prior to isotherm data collection. Adsorption points in the pressure range 0.003-0.015 bar were used for BET surface area evaluation. DRIFTS data were recorded on a Nicolet 6700 FTIR spectrometer equipped with a MCT detector that was cooled to 77 K. The spectra were collected in a KBr mixture under argon purge (samples prepared in air). Pure KBr was measured as the background and subtracted from sample spectra. FTIR data

were recorded on a Nicolet iS10 from Thermo Scientific. <sup>1</sup>H-NMR data were recorded on Avance DMX-400 from Bruker. SEM images were collected using a JEOL 7900. XPS measurements were performed using a Thermo Scientific ESCALAB 250 Xi equipped with an electron flood gun and a scanning ion gun. Thermo Scientific Avantage Data System software was used for data analysis with the C 1s peak at 284.8 eV used as reference.

Adsorption testing details. Adsorption studies were performed by adding 10-50 mg of NU-1000 to 50 mL of PFAS solution (single compound, lab mixture or groundwater sample) in a 50 mL polypropylene tube on a tumbler at 150 rpm and room temperature. After tumbling for 30 min, the solution was filtered with a 0.25 µm nylon membrane and diluted using methanol for analysis. The groundwater samples were collected from monitoring wells in fire training areas, burn pits, and various other water sources as a part of completed field investigations at U.S. Air Force installations. The samples were labeled as IDW 1 through IDW 4 to maintain the confidentiality of sample locations. All experiments were performed in duplicate and average values were reported.

Regeneration testing details. Regeneration studies were performed by adding 100 mg of NU-1000 to 50 mL of 10 or 1000 mg/L PFBS solution before it was placed on a tumbler at 150 rpm at room temperature. The solution was centrifuged after 30 min at 6000 rpm for 10 min at room temperature. The supernatant was collected, filtered, diluted, and analyzed for PFBS. The residual saturated solid adsorbent was placed in 10 mL regeneration solvent (e.g., 30/70 v/v 0.1 M HCl/methanol) followed by 30 min sonication and 30 min shaking at room temperature. The regeneration solvent with adsorbent was then centrifuged at 6000 rpm for 10 min at room temperature and the supernatant collected. This procedure was repeated 3 times and the collected supernatants were combined and filtered through a 0.25 μm nylon membrane followed by dilution using methanol before analysis. The regenerated adsorbent was dried in nitrogen for 30 min before the next adsorption run. All experiments were performed in duplicate and average values were reported.

**PFAS analysis details.** PFAS concentrations were analyzed as previously reported<sup>5</sup> in negative ionization mode using UPLC-MS-MS (Thermo Scientific, Vanquish-TSQ ALTIS) equipped with Waters Acquity HSS T3 column (2.1 mm  $\times$  100 mm, 1.8  $\mu$ m). Samples were diluted with methanol, then sonicated and centrifuged prior to injection (20  $\mu$ L).

**Computational methods.** DFT calculations were performed using the PWscf package within Quantum Espresso. 43-44 vdW-DF2 exchange correlation function was used to account for van der Waals interactions which play a vital role in modeling guest molecule—MOF bonding. 45-47 In addition, ultrasoft pseudopotentials with a plane wave basis set using kinetic energy cutoffs of 50 and 500 Ry were used for wavefunctions and charge density, respectively. 48 Geometry optimization of the nuclear coordinates were

performed using the Broyden-Fletcher-Golfarb-Shanno algorithm until the smallest force component did not exceed  $2.6 \times 10^{-2} \, \text{eV/Å}$ .

### SUPPORTING INFORMATION

The Supporting Information is available free of charge on the ACS Publications website at DOI: 10.1021/acs.chemmaterXXX.

Concentration profiles of PFAS as function of time; adsorption capacity and isotherms; SEM images; PFBS removal using different MOFs; DTF optimized geometries of PFAS@NU-1000; recovery of PFBS; PXRD patterns and N<sub>2</sub> isotherms after regeneration; NMR spectra of NU-1000; PXRD patterns of NU-1000 after adsorption of IDW samples; current literature overview of PFAS@MOF adsorption characteristics; PFAS analytes; comparison of different adsorbents for PFAS removal; PFAS concentration in lab-prepared mixture and IDW water samples; XPS binding energies of PFBS@NU-1000.

#### **ACKNOWLEDGEMENTS**

M.W. gratefully acknowledges the National Science Foundation CAREER Program (Award No. 1752771) for support of this research. R.S. and D.J.T. acknowledges support from the Extreme Science and Engineering Discovery Environment (XSEDE), which is supported by National Science Foundation grant number TG-CHE190008. R.L. thanks Dr. Daniel Andreescu for the assistance in FTIR characterization. M.C.W. is supported by the NSF Graduate Research Fellowship under grant DGE-1842165. O.K.F. and T.I. gratefully acknowledge the support of the Nanoporous Materials Genome Center, funded by the US Department of Energy (DOE), Office of Science, Basic Energy Sciences Program (award DE-FG02-17ER16362). T.M.H. acknowledges the support of Center for Air and Aquatic Resources Engineering and Sciences (CAARES), which is accredited to perform PFAS analysis by the Department of Defense Environmental Laboratory Accreditation Program (DoD ELAP).

## **REFERENCES**

1. Zhang, D. Q.; Zhang, W. L.; Liang, Y. N., Adsorption of perfluoroalkyl and polyfluoroalkyl substances (PFASs) from aqueous solution - A review. *Sci. Total Environ.* **2019**, *694*, 133606.

- 2. Li, R.; Munoz, G.; Liu, Y.; Sauvé, S.; Ghoshal, S.; Liu, J., Transformation of novel polyfluoroalkyl substances (PFASs) as co-contaminants during biopile remediation of petroleum hydrocarbons. *J. Hazard. Mater.* **2019**, *362*, 140-147.
- 3. Rahman, M. F.; Peldszus, S.; Anderson, W. B., Behaviour and fate of perfluoroalkyl and polyfluoroalkyl substances (PFASs) in drinking water treatment: A review. *Water Res.* **2014**, *50*, 318-340.
- 4. Clark, C. A.; Heck, K. N.; Powell, C. D.; Wong, M. S., Highly Defective UiO-66 Materials for the Adsorptive Removal of Perfluorooctanesulfonate. *ACS Sustain. Chem. Eng.* **2019**, *7*, 6619-6628.
- 5. Singh, R. K.; Multari, N.; Nau-Hix, C.; Anderson, R. H.; Richardson, S. D.; Holsen, T. M.; Mededovic Thagard, S., Rapid Removal of Poly- and Perfluorinated Compounds from Investigation-Derived Waste (IDW) in a Pilot-Scale Plasma Reactor. *Environ. Sci. Technol.* **2019**, *53*, 11375-11382.
- 6. Lu, D.; Sha, S.; Luo, J.; Huang, Z.; Zhang Jackie, X., Treatment train approaches for the remediation of per- and polyfluoroalkyl substances (PFAS): A critical review. *J. Hazard. Mater.* **2020**, *386*, 121963.
- 7. McCleaf, P.; Englund, S.; Östlund, A.; Lindegren, K.; Wiberg, K.; Ahrens, L., Removal efficiency of multiple poly- and perfluoroalkyl substances (PFASs) in drinking water using granular activated carbon (GAC) and anion exchange (AE) column tests. *Water Res.* **2017**, *120*, 77-87.
- 8. Ateia, M.; Maroli, A.; Tharayil, N.; Karanfil, T., The overlooked short- and ultrashort-chain poly- and perfluorinated substances: A review. *Chemosphere* **2019**, *220*, 866-882.
- 9. Brendel, S.; Fetter, É.; Staude, C.; Vierke, L.; Biegel-Engler, A., Short-chain perfluoroalkyl acids: environmental concerns and a regulatory strategy under REACH. *Environ. Sci. Eur.* **2018**, *30*, 9.
- 10. Zhao, P.; Xia, X.; Dong, J.; Xia, N.; Jiang, X.; Li, Y.; Zhu, Y., Short- and long-chain perfluoroalkyl substances in the water, suspended particulate matter, and surface sediment of a turbid river. *Sci. Total Environ.* **2016**, *568*, 57-65.
- 11. Arvaniti, O. S.; Stasinakis, A. S., Review on the occurrence, fate and removal of perfluorinated compounds during wastewater treatment. *Sci. Total Environ.* **2015**, *524-525*, 81-92.
- 12. Gagliano, E.; Sgroi, M.; Falciglia, P. P.; Vagliasindi, F. G. A.; Roccaro, P., Removal of poly- and perfluoroalkyl substances (PFAS) from water by adsorption: Role of PFAS chain length, effect of organic matter and challenges in adsorbent regeneration. *Water Res.* **2019**, *171*, 115381.

- 13. Appleman, T. D.; Dickenson, E. R. V.; Bellona, C.; Higgins, C. P., Nanofiltration and granular activated carbon treatment of perfluoroalkyl acids. *J. Hazard. Mater.* **2013**, *260*, 740-746.
- 14. Chen, Z.; Li, P.; Anderson, R.; Wang, X.; Zhang, X.; Robison, L.; Redfern, L. R.; Moribe, S.; Islamoglu, T.; Gómez-Gualdrón, D. A.; Yildirim, T.; Stoddart, J. F.; Farha, O. K., Balancing volumetric and gravimetric uptake in highly porous materials for clean energy. *Science* 2020, 368, 297-303.
- 15. Li, P.; Vermeulen, N. A.; Malliakas, C. D.; Gómez-Gualdrón, D. A.; Howarth, A. J.; Mehdi, B. L.; Dohnalkova, A.; Browning, N. D.; O'Keeffe, M.; Farha, O. K., Bottom-up construction of a superstructure in a porous uranium-organic crystal. *Science* **2017**, *356*, 624-627.
- 16. Deng, H.; Grunder, S.; Cordova, K. E.; Valente, C.; Furukawa, H.; Hmadeh, M.; Gándara, F.; Whalley, A. C.; Liu, Z.; Asahina, S.; Kazumori, H.; O'Keeffe, M.; Terasaki, O.; Stoddart, J. F.; Yaghi, O. M., Large-Pore Apertures in a Series of Metal-Organic Frameworks. *Science* 2012, 336, 1018-1023.
- 17. DeCoste, J. B.; Peterson, G. W., Metal-Organic Frameworks for Air Purification of Toxic Chemicals. *Chem. Rev.* **2014**, *114*, 5695-5727.
- 18. Mon, M.; Bruno, R.; Ferrando-Soria, J.; Armentano, D.; Pardo, E., Metal—organic framework technologies for water remediation: towards a sustainable ecosystem. *J. Mater. Chem. A* **2018**, *6*, 4912-4947.
- 19. Drout, R. J.; Robison, L.; Chen, Z.; Islamoglu, T.; Farha, O. K., Zirconium Metal–Organic Frameworks for Organic Pollutant Adsorption. *Trends Chem.* **2019**, *1*, 304-317.
- 20. Bobbitt, N. S.; Mendonca, M. L.; Howarth, A. J.; Islamoglu, T.; Hupp, J. T.; Farha, O. K.; Snurr, R. Q., Metal–organic frameworks for the removal of toxic industrial chemicals and chemical warfare agents. *Chem. Soc. Rev.* **2017**, *46*, 3357-3385.
- Liu, K.; Zhang, S.; Hu, X.; Zhang, K.; Roy, A.; Yu, G., Understanding the Adsorption of PFOA on MIL-101(Cr)-Based Anionic-Exchange Metal—Organic Frameworks: Comparing DFT Calculations with Aqueous Sorption Experiments. *Environ. Sci. Technol.* 2015, 49, 8657-8665.
- 22. Barpaga, D.; Zheng, J.; Han, K. S.; Soltis, J. A.; Shutthanandan, V.; Basuray, S.; McGrail, B. P.; Chatterjee, S.; Motkuri, R. K., Probing the Sorption of Perfluorocatanesulfonate Using Mesoporous Metal-Organic Frameworks from Aqueous Solutions. *Inorg. Chem.* 2019, 58, 8339-8346.

- 23. Sini, K.; Bourgeois, D.; Idouhar, M.; Carboni, M.; Meyer, D., Metal-organic framework sorbents for the removal of perfluorinated compounds in an aqueous environment. *New J. Chem.* **2018**, *42*, 17889-17894.
- 24. Chen, M.-J.; Yang, A.-C.; Wang, N.-H.; Chiu, H.-C.; Li, Y.-L.; Kang, D.-Y.; Lo, S.-L., Influence of crystal topology and interior surface functionality of metal-organic frameworks on PFOA sorption performance. *Microporous Mesoporous Mater.* **2016**, *236*, 202-210.
- 25. Li, Y.; Yang, Z.; Wang, Y.; Bai, Z.; Zheng, T.; Dai, X.; Liu, S.; Gui, D.; Liu, W.; Chen, M.; Chen, L.; Diwu, J.; Zhu, L.; Zhou, R.; Chai, Z.; Albrecht-Schmitt, T. E.; Wang, S., A mesoporous cationic thorium-organic framework that rapidly traps anionic persistent organic pollutants. *Nat. Commun.* 2017, 8, 1354.
- Howarth, A. J.; Katz, M. J.; Wang, T. C.; Platero-Prats, A. E.; Chapman, K. W.; Hupp, J. T.; Farha, O. K., High Efficiency Adsorption and Removal of Selenate and Selenite from Water Using Metal–Organic Frameworks. J. Am. Chem. Soc. 2015, 137, 7488-7494.
- 27. Hou, J.; Wang, H.; Zhang, H., Zirconium Metal-Organic Framework Materials for Efficient Ion Adsorption and Sieving. *Ind. Eng. Chem. Res.* **2020**, *59*, 12907-12923.
- 28. Bai, Y.; Dou, Y.; Xie, L.-H.; Rutledge, W.; Li, J.-R.; Zhou, H.-C., Zr-based metal—organic frameworks: design, synthesis, structure, and applications. *Chem. Soc. Rev.* **2016**, *45*, 2327-2367.
- 29. Mondloch, J. E.; Bury, W.; Fairen-Jimenez, D.; Kwon, S.; DeMarco, E. J.; Weston, M. H.; Sarjeant, A. A.; Nguyen, S. T.; Stair, P. C.; Snurr, R. Q.; Farha, O. K.; Hupp, J. T., Vapor-Phase Metalation by Atomic Layer Deposition in a Metal-Organic Framework. *J. Am. Chem. Soc.* **2013**, *135*, 10294-10297.
- 30. Islamoglu, T.; Otake, K.-i.; Li, P.; Buru, C. T.; Peters, A. W.; Akpinar, I.; Garibay, S. J.; Farha, O. K., Revisiting the structural homogeneity of NU-1000, a Zr-based metal—organic framework. CrystEngComm 2018, 20, 5913-5918.
- 31. Xiao, L.; Ching, C.; Ling, Y.; Nasiri, M.; Klemes, M. J.; Reineke, T. M.; Helbling, D. E.; Dichtel, W. R., Cross-linker Chemistry Determines the Uptake Potential of Perfluorinated Alkyl Substances by β-Cyclodextrin Polymers. *Macromolecules* **2019**, *52*, 3747-3752.
- 32. Du, Z.; Deng, S.; Bei, Y.; Huang, Q.; Wang, B.; Huang, J.; Yu, G., Adsorption behavior and mechanism of perfluorinated compounds on various adsorbents—A review. *J. Hazard. Mater.* **2014**, *274*, 443-454.

- 33. Aulakh, D.; Liu, L.; Varghese, J. R.; Xie, H.; Islamoglu, T.; Duell, K.; Kung, C.-W.; Hsiung, C.-E.; Zhang, Y.; Drout, R. J.; Farha, O. K.; Dunbar, K. R.; Han, Y.; Wriedt, M., Direct Imaging of Isolated Single-Molecule Magnets in Metal–Organic Frameworks. *J. Am. Chem. Soc.* **2019**, *141*, 2997-3005.
- 34. Aulakh, D.; Pyser, J. B.; Zhang, X.; Yakovenko, A. A.; Dunbar, K. R.; Wriedt, M., Metal-Organic Frameworks as Platforms for the Controlled Nanostructuring of Single-Molecule Magnets. *J. Am. Chem. Soc.* **2015**, *137*, 9254-9257.
- 35. Aulakh, D.; Xie, H.; Shen, Z.; Harley, A.; Zhang, X.; Yakovenko, A. A.; Dunbar, K. R.; Wriedt, M., Systematic Investigation of Controlled Nanostructuring of Mn12 Single-Molecule Magnets Templated by Metal–Organic Frameworks. *Inorg. Chem.* **2017**, *56*, 6965-6972.
- 36. Islamoglu, T.; Ray, D.; Li, P.; Majewski, M. B.; Akpinar, I.; Zhang, X.; Cramer, C. J.; Gagliardi, L.; Farha, O. K., From Transition Metals to Lanthanides to Actinides: Metal-Mediated Tuning of Electronic Properties of Isostructural Metal-Organic Frameworks. *Inorg. Chem.* **2018**, *57*, 13246-13251.
- 37. Dietzel, P. D. C.; Blom, R.; Fjellvåg, H., Base-Induced Formation of Two Magnesium Metal-Organic Framework Compounds with a Bifunctional Tetratopic Ligand. *Eur. J. Inorg. Chem.* **2008**, *2008*, 3624-3632.
- 38. Cavka, J. H.; Jakobsen, S.; Olsbye, U.; Guillou, N.; Lamberti, C.; Bordiga, S.; Lillerud, K. P., A New Zirconium Inorganic Building Brick Forming Metal Organic Frameworks with Exceptional Stability. J. Am. Chem. Soc. 2008, 130, 13850-13851.
- 39. Park, K. S.; Ni, Z.; Côté, A. P.; Choi, J. Y.; Huang, R.; Uribe-Romo, F. J.; Chae, H. K.; O'Keeffe, M.; Yaghi, O. M., Exceptional chemical and thermal stability of zeolitic imidazolate frameworks. *Proc. Natl. Acad. Sci. U.S.A.* **2006**, *103*, 10186-10191.
- 40. Kato, S.; Otake, K.-i.; Chen, H.; Akpinar, I.; Buru, C. T.; Islamoglu, T.; Snurr, R. Q.; Farha, O. K., Zirconium-Based Metal—Organic Frameworks for the Removal of Protein-Bound Uremic Toxin from Human Serum Albumin. *J. Am. Chem. Soc.* **2019**, *141*, 2568-2576.
- 41. Punyapalakul, P.; Suksomboon, K.; Prarat, P.; Khaodhiar, S., Effects of Surface Functional Groups and Porous Structures on Adsorption and Recovery of Perfluorinated Compounds by Inorganic Porous Silicas. *Sep. Sci. Technol.* **2013**, *48*, 775-788.

- 42. Yang, D.; Bernales, V.; Islamoglu, T.; Farha, O. K.; Hupp, J. T.; Cramer, C. J.; Gagliardi, L.; Gates, B. C., Tuning the Surface Chemistry of Metal Organic Framework Nodes: Proton Topology of the Metal-Oxide-Like Zr6 Nodes of UiO-66 and NU-1000. *J. Am. Chem. Soc.* **2016**, *138*, 15189-15196.
- 43. Giannozzi, P.; Baroni, S.; Bonini, N.; Calandra, M.; Car, R.; Cavazzoni, C.; Ceresoli, D.; Chiarotti, G. L.; Cococcioni, M.; Dabo, I.; Dal Corso, A.; de Gironcoli, S.; Fabris, S.; Fratesi, G.; Gebauer, R.; Gerstmann, U.; Gougoussis, C.; Kokalj, A.; Lazzeri, M.; Martin-Samos, L.; Marzari, N.; Mauri, F.; Mazzarello, R.; Paolini, S.; Pasquarello, A.; Paulatto, L.; Sbraccia, C.; Scandolo, S.; Sclauzero, G.; Seitsonen, A. P.; Smogunov, A.; Umari, P.; Wentzcovitch, R. M., QUANTUM ESPRESSO: a modular and open-source software project for quantum simulations of materials. *J. Phys. Condens. Matter.* 2009, 21, 395502.
- 44. Giannozzi, P.; Andreussi, O.; Brumme, T.; Bunau, O.; Buongiorno Nardelli, M.; Calandra, M.; Car, R.; Cavazzoni, C.; Ceresoli, D.; Cococcioni, M.; Colonna, N.; Carnimeo, I.; Dal Corso, A.; de Gironcoli, S.; Delugas, P.; DiStasio, R. A.; Ferretti, A.; Floris, A.; Fratesi, G.; Fugallo, G.; Gebauer, R.; Gerstmann, U.; Giustino, F.; Gorni, T.; Jia, J.; Kawamura, M.; Ko, H. Y.; Kokalj, A.; Küçükbenli, E.; Lazzeri, M.; Marsili, M.; Marzari, N.; Mauri, F.; Nguyen, N. L.; Nguyen, H. V.; Otero-de-la-Roza, A.; Paulatto, L.; Poncé, S.; Rocca, D.; Sabatini, R.; Santra, B.; Schlipf, M.; Seitsonen, A. P.; Smogunov, A.; Timrov, I.; Thonhauser, T.; Umari, P.; Vast, N.; Wu, X.; Baroni, S., Advanced capabilities for materials modelling with Quantum ESPRESSO. J. Phys. Condens. Matter. 2017, 29, 465901.
- 45. Langreth, D. C.; Lundqvist, B. I.; Chakarova-Käck, S. D.; Cooper, V. R.; Dion, M.; Hyldgaard, P.; Kelkkanen, A.; Kleis, J.; Kong, L.; Li, S.; Moses, P. G.; Murray, E.; Puzder, A.; Rydberg, H.; Schröder, E.; Thonhauser, T., A density functional for sparse matter. *J. Phys. Condens. Matter.* **2009**, *21*, 084203.
- 46. Zuluaga, S.; Canepa, P.; Tan, K.; Chabal, Y. J.; Thonhauser, T., Study of van der Waals bonding and interactions in metal organic framework materials. *J. Phys. Condens. Matter.* **2014**, *26*, 133002.
- 47. Thonhauser, T.; Cooper, V. R.; Li, S.; Puzder, A.; Hyldgaard, P.; Langreth, D. C., Van der Waals density functional: Self-consistent potential and the nature of the van der Waals bond. *Phys. Rev. B* **2007**, *76*, 125112.
- 48. Vanderbilt, D., Soft self-consistent pseudopotentials in a generalized eigenvalue formalism. *Phys. Rev. B* **1990**, *41*, 7892-7895.

# **Graphical Abstract**

